2D Materials

PAPER

Silicene's pervasive surface alloy on Ag(111): a scaffold for two-dimensional growth

Johannes T Küchle[1,2], Aleksandr Baklanov[1], Ari P Seitsonen[3,4], Paul T P Ryan[2,5,7], Peter Feulner[1], Prashanth Pendem[1], Tien-Lin Lee[2], Matthias Muntwiler[6], Martin Schwarz[1], Felix Haag[1], Johannes V Barth[1], Willi Auwärter[1], David A Duncan[1,2,*] and Francesco Allegretti[1,*]

[1] Physics Department E20, Technical University of Munich, D-85748 Garching, Germany
[2] Diamond Light Source, Harwell Science and Innovation Campus, Didcot OX11 0DE, United Kingdom
[3] Département de Chimie, École Normale Supérieure, F-75005 Paris, France
[4] Université Paris Sciences et Lettres, Sorbonne Université, Centre National de la Recherche Scientifique, F-75005 Paris, France
[5] Department of Materials, Imperial College London, South Kensington, London SW7 2AZ, United Kingdom
[6] Paul Scherrer Institut, Villigen CH-5232, Switzerland
[7] Present address: Institute of Applied Physics, Technische Universität Wien, A-1040 Vienna, Austria.
[*] Authors to whom any correspondence should be addressed.

E-mail: david.duncan@diamond.ac.uk **and** francesco.allegretti@ph.tum.de

Keywords: 2D materials, epitaxial growth, silicene, alloy, x-ray photoelectron spectroscopy, x-ray standing waves, scanning tunneling microscopy

Supplementary material for this article is available online

OPEN ACCESS

RECEIVED
2 June 2022

REVISED
8 August 2022

ACCEPTED FOR PUBLICATION
15 August 2022

PUBLISHED
6 September 2022

Abstract

Silicene, the two-dimensional (2D) allotrope of silicon, is a promising material for electronics. So far, the most direct synthesis strategy has been to grow it epitaxially on metal surfaces; however, the effect of the strong silicon-metal interaction on the structure and electronic properties of the metal-supported silicene is generally poorly understood. In this work, we consider the (4×4)-silicene monolayer (ML) grown on Ag(111), probably the most illustrious representative of the 2D silicon family, and show that our experimental results refute the common interpretation of this system as a simple buckled, honeycomb ML with a sharp interface to the Ag substrate. Instead, the presented analysis demonstrates the pervasive presence of a second silicon species, which we conclude to be a Si–Ag alloy stacked between the 2D silicene and the silver substrate and scaffolding the 2D silicene layer. These findings question the current structural understanding of the silicene/Ag(111) interface and may raise expectations of analogous alloy systems in the stabilization of other 2D materials grown epitaxially on metal surfaces.

1. Introduction

Graphene has captivated the world's attention for its various outstanding physical and electronic properties. However, the lack of a band gap limits graphene's utilization within electronics. There has been extensive research aimed at inducing a band gap [1–3], but these efforts often affect the 'outstanding' properties [4]. Silicene, the silicon analogue of graphene, was predicted to exhibit an electrically tunable band gap [5, 6], with similarly attractive properties [7]. Multiple silicene phases have been discovered, first on Ag(111) [8, 9] and subsequently on other substrates [10], yet the most studied is the (4×4) phase on Ag(111) [11]—the first phase claimed to exhibit a Dirac-like dispersion [11]. While this claim was later refuted [12], the presence of Dirac cones was observed for other silicene phases [13]. Nevertheless, the issue remains controversial for the Ag-supported monolayers (MLs) [14] due to strong interactions with the silver substrate, which are invoked for both the appearance [15] or absence [12, 16, 17] of the cone structure. Understanding the nature of the interaction between the silicene and the surface is therefore essential to develop silicene-based electronics.

The currently accepted structure of the (4×4) phase has the Si atoms laterally arranged in a honeycomb lattice with one third of the atoms displaced above the lower two thirds with an atomic buckling of $0.75 - 0.84$ Å [18–21] (figures 1(a) and (b)). This

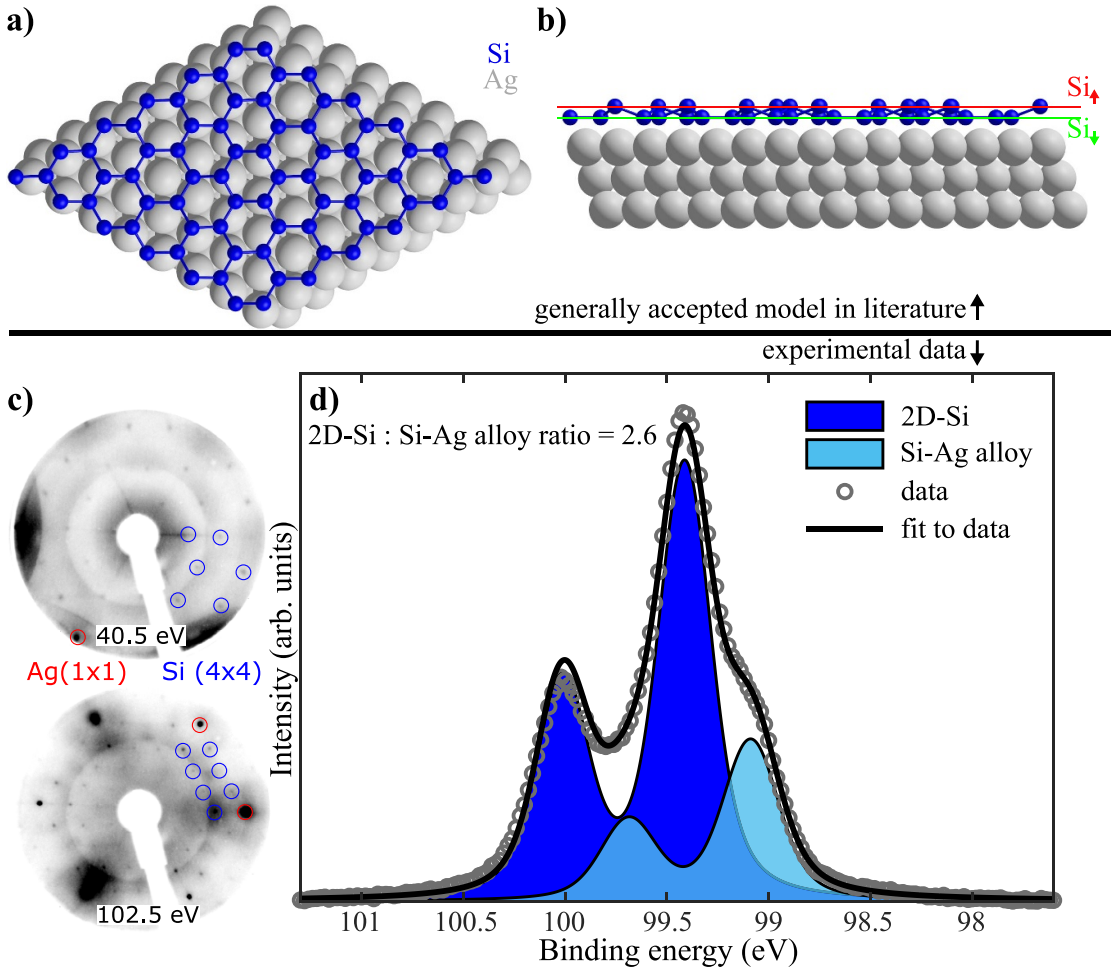

Figure 1. Literature model (a), (b), LEED (c), and HR-XPS signature (d) of investigated (4×4)-silicene/Ag(111). (a) Top and (b) side view of the buckled honeycomb model that is currently accepted in literature (Si atoms are represented as blue spheres, Ag atoms as grey spheres). (c) LEED patterns demonstrating the purity and long-range order of the (4×4) superstructure investigated by HR-XPS and NIXSW at the Diamond Light Source. (d) Si 2p HR-XP spectrum (photon energy: 250 eV). The assignment of the two spin–orbit doublets at higher (blue, Si $2p_{3/2}$ at 99.4 eV) and lower BE (light blue, Si $2p_{3/2}$ at 99.1 eV) to 2D-Si and alloy species is discussed in the text. Coverage is estimated to be roughly 0.3 ML (*vide infra*) based on the 2D-Si: Si–Ag alloy ratio, as shown in figure 2.

structure was repeatedly predicted by density functional theory (DFT) [11, 21–24] and experimentally determined using quantitative low-energy electron diffraction (LEED-IV) [19], reflection high-energy positron diffraction (RHEPD) [18], surface x-ray diffraction (SXRD) [20], and atomic force microscopy (AFM) [21]. However, our work demonstrates that this model is too simplistic and a silicon–silver alloy beneath the two-dimensional (2D) silicene layer needs to be considered.

Strong interactions between silver and silicon are well established (e.g. [25–27]), with some reports of Ag–Si intermixing in silicene [28, 29]. Furthermore, alloying between silver and most group IV elements is well established (e.g. [30–33]). Thus, it is surprising that no Si–Ag alloy has been explicitly considered in the structural models of silicene MLs on Ag(111), in particular because the insertion and the exchange of Si atoms into or with Ag has been demonstrated [34–36]. Strikingly, tin's silicene-analogue, stanene, was revealed to grow on an alloyed, rather than bulk-terminated, Ag(111) surface [32].

In this light, we re-investigated the atomic structure of (4×4)-silicene using a suite of techniques with structural and chemical sensitivity and conclude that there is only one natural explanation for our observations: a Si–Ag alloy underpins silicene growth. High resolution x-ray photoelectron spectroscopy (HR-XPS) demonstrates two distinct silicon species, one attributed to silicene, the other dominant at low coverage, both of which persist after the (4×4) phase forms. Comparative Ge studies hint that this second species is a Si–Ag alloy. Normal incidence x-ray standing wave (NIXSW) experiments are not consistent with the literature (4×4)-silicene models and necessitate an additional structural motif: surface-incorporated Si. Scanning tunneling microscopy (STM) identifies a new Si/Ag(111) phase near (4×4)-silicene, suggesting Si–Ag alloy intrusions upon which the (4×4) phase grows. Finally, DFT

calculations demonstrate that literature models cannot explain our results, underlining the need to re-evaluate the current understanding of the (4×4) phase, and perhaps all silicene phases, on the Ag(111) surface.

2. Methods

2.1. Preparations

Sample preparation was conducted by repeated cycles of Ar^+ sputtering at 1 kV and annealing *in vacuo* at 725 K. For Si evaporation, a high-quality Si wafer was resistively heated using a custom-built evaporator, generating a flux of elemental Si. The evaporator consists of two water-cooled Cu electrodes, between which the Si wafer is mounted, and a current is passed through. Ge was evaporated using a similar custom-built evaporator, modified to heat a Ta crucible filled with small Ge flakes, thus yielding a pure Ge flux. The Ag(111) substrate was kept at 550 K during Si evaporation and 450 K during Ge evaporation. The preparation conditions (i.e. substrate temperature, evaporation rate and evaporation time) were optimized to obtain largely single-phase silicene with (4×4) periodicity, and the rectangular $c\left(\sqrt{3} \times 7\right)$ superstructure of quasi freestanding germanene, respectively, as judged by LEED or STM. The measured evaporation rate for the silicene evaporation during the growth of the (4×4) overlayer was $\sim$4 pm min^{-1}, based on a quartz microbalance placed approximately equidistant to the sample, behind the evaporant. This rate was obtained after an extensive growth study. The measurements were performed in three different experimental stations, all with base pressure in the low 10^{-10} mbar range. Note that the synchrotron endstations (see below) lack a thermocouple mounted directly at the sample, hence, there is an unavoidable uncertainty in the precise substrate temperature. Comparability of the samples at different experimental stations was ensured via a quartz crystal microbalance monitoring the deposited amount and verified via LEED. The difficulties in the precise reproducibility of the distance between the sample and the evaporator yields an uncertainty of about $\pm 10\%$ on the evaporated amount.

In the following, the coverage is assigned in fractions of MLs, where we use the same definition of 1 ML as [37], namely corresponding to the completion of the Si wetting layer.

2.2. Experimental techniques

The high-resolution XPS measurements for the coverage dependence of the Si 2p core-level signatures were performed at the X03DA beamline (PEARL) of the Swiss Light Source (SLS) in Switzerland [38]. The HR-XPS data were acquired at room temperature in normal emission geometry, and the binding energy (BE) scale was calibrated against the Fermi edge. The curve-fitting analysis was performed using a convolution of Doniach-Sunjic and Gaussian line shapes superimposed on a background built of a constant, a linear component, and a step-function. For each Si 2p spin–orbit doublet, a spin–orbit splitting of 0.6 eV [39, 40] and a branching ratio $I(2p_{3/2}):I(2p_{1/2}) = 2:1$ (defined in terms of peak areas) were used. For all individual components the full-widths at half maximum (FWHM) were fixed at a similar value of 0.32 eV and only slightly optimized for distinct spin–orbit doublets. The determined ratio between the two-dimensional Si species (2D-Si) and Si–Ag alloy components (*vide infra*) reflects a convolution of the actual amount of 2D-Si present on the surface and the attenuation of the lower-lying Si–Ag alloy phase. However, we do not expect this attenuation to have a significant impact on the precise ratio at normal emission. In any case, it does not change the trend of the increasing ratio.

NIXSW and HR-XPS spectra of the (4×4) phase of silicene were recorded at the beamline I09 [41] of the Diamond Light Source (United Kingdom), which can deliver both hard (2.1–20 keV) and soft (120–2100 eV) x-rays to the same spot on the sample. The NIXSW technique exploits the standing wavefield generated by the interference between the incident and reflected x-rays at the Bragg condition. The period of this standing wave matches the interplanar spacing (d_{hkl}) between the Bragg diffraction planes [42]. In the case of Ag(111), the Bragg diffraction planes of the (111) and the $(\bar{1}11)$ reflections are coincident with the atomic planes with a layer spacing of $d_{111} = 2.36$ Å. Importantly, the phase of the standing wave, and thus the location of its maximum intensity with respect to the Bragg diffraction planes, varies as the photon energy is scanned through the Bragg condition. Any atom immersed in this standing wavefield will experience a varying electromagnetic field intensity as a function of the photoelectron energy and depending on its position between these diffraction planes, resulting in a characteristic x-ray absorption or photoelectron intensity profile. The measured profile is then fitted uniquely, using dynamical diffraction theory [43], by two dimensionless structure parameters [44]: the coherent fraction, f^{hkl}, and the coherent position, p^{hkl}. These broadly correspond to, respectively, the degree of order and the mean position (in units of d_{hkl}) of the absorber atoms relative to the Bragg diffraction planes. By measuring NIXSW data at different Bragg reflections (h,k,l), one can use the values of f^{hkl} and p^{hkl} to triangulate the position of emitter atoms with respect to the underlying crystal [44]. Here, we use the $(\bar{1}11)$ reflection (70.5° inclination from the surface plane) for triangulation. In particular, the NIXSW experiments were conducted by monitoring the Si 1s core level while scanning the photon energy across the Bragg reflection of the (111) and $(\bar{1}11)$ planes at 2.639 keV. Prior to the

scan, the x-ray reflectivity was measured to determine the Bragg energy, which was varied in the range of ±5 eV to acquire the scan. The measurements were taken at four unique spots for each reflection, the results averaged to improve the signal-to-noise ratio, and the uncertainty determined by taking the standard error in the fit at two standard deviations. As with the XPS, the peaks of individual spectra of the NIXSW were fitted using a convolution of Doniach-Sunjic and Gaussian profiles on a background consisting of a constant, a linear slope, and a step-function. All fitting parameters, beside the intensity and the background, were optimized before the final fitting and then fixed, to allow only the intensity to be varied over the photon energy range. As the FWHM is fixed, the intensity of each peak was assumed to be directly proportional to the area and therefore to the photoemission yield. To account for non-dipolar effects in the angular dependence in the NIXSW an asymmetry factor, Q, was used. Q was calculated theoretically using the average angle θ as defined in [45] and weighted by the emission intensity at an off-Bragg energy ($\theta = 18°$ for the (111) reflection and $\theta = 15°$ for the $(\bar{1}11)$ reflection). The vibrational amplitudes were calculated using the Debye temperatures of Si (692 K) and Ag (221 K) and the experimental temperature (100 K) to be 0.033 Å for Si and 0.053 Å for Ag. Assuming that the two vibrations are uncoupled results in a net root-mean-square vibrational amplitude of 0.062 Å; this yields an estimated Debye–Waller factor of $F_{DW} = 0.986$ [46]. The ordered fraction (C) of the substrate is assumed to be 1. The corrected coherent fractions are then calculated from the experimentally extracted value as $f_{coh} = f_{extracted}/(F_{DW} \cdot C)$ [44]. At off-Bragg energies, the Si 1s core level appears as a single broad peak, however, as we scan across the Bragg peak, it becomes clear that the line shape of the Si 1s changes as a function of the photon energy (cf. supplementary information, SI, §1, figure S1), which clearly indicates the presence of two chemically unique species in the Si 1s, as are observed in the Si 2p XPS. Additionally, it also shows that the two species differ structurally, as they result in significantly different yield profiles. Importantly, the chemical shift of 0.25 eV matches the XPS analysis for the Si 2p core level.

Both PEARL and beamline I09 utilize a Scienta EW4000 hemispherical analyzer to detect photoelectrons. At beamline I09 the analyzer is mounted perpendicular to the incident light in the plane of the photon polarization (linear horizontal), with the analyzer entrance slit also parallel to this plane. At PEARL the analyzer is mounted at a 60° angle with respect to the incident light (linear horizontal), also in the plane of the photon polarization, with the analyzer entrance slit perpendicular to this plane. Section 2 in the SI details which XP spectra were acquired at either PEARL or beamline I09.

The STM measurements were conducted using a CreaTec instrument in a custom-designed UHV system at the Physics Department E20 of the Technical University of Munich (Garching, Germany). Electrochemically etched tungsten tips were used, and all images were acquired at 6 K in the constant-current mode of operation. The Ag(111) crystal close-packed directions were determined with an accuracy of ∼4° by atomically resolving the crystal lattice, imaging surface dislocations and considering unit cell rotations of known silicene superstructures. The lateral dimensions were similarly calibrated.

2.3. Theoretical calculations

The DFT [47] calculations were performed using the approximation B86r-vdW-DF2 [48] to the exchange-correlation term. The specific choice of the B86r-vdW-DF2 functional has been taken based on our recent extensive testing of the h-BN/Ir(111) and graphene/Ir(111) moiré structures [49] and other similar structures, such as h-BN/Rh(111) and h-BN/Ni(111). The computed lattice constant 4.1075 Å was used in the calculations. The slab geometry was applied, with 12–13 Å of vacuum between the consecutive replicas of the slab. Five layers of the substrate, with the two lowest layers fixed at the bulk geometry, were used leading to 98 atoms in most of the computed models. The different asymptotic potentials from the opposing surfaces were treated with a surface dipole-correction. A Γ point-centered 6 × 6 mesh of equidistant k points [50] was used to approximate the integration over the first Brillouin zone, and the occupation numbers were broadened with a Fermi–Dirac function with a width of 50 meV. The projector augmented wave (PAW) method [51] was used to avoid the explicit treatment of the core orbitals in the calculations. The STM images were simulated using the Tersoff–Hamann model [52], at the bias voltage of −0.3 eV.

The Quantum ESPRESSO (QE) suite of codes [53] was employed in the calculations, and the van der Waals functional implemented as described in [54]. The wave functions were expanded in a basis set of 50 Ry and the density at 400 Ry. The PAW datasets were taken from the Pslibrary [55]. The code Vienna *Ab initio* Simulation Package [56] was used to evaluate the core level BEs, within the final state approximation, in the geometries obtained from the QE code suite.

The simulated coherent fraction and position values (tables 1 and S2, S3) for the comparison to NIXSW were calculated as described in [44]. Specifically, the coherent position was calculated as the mean of the position of the Si atoms, and the coherent fraction was calculated using equation (16) of [44]. For the geometrical variations, the upwards buckled Si layer, or the entire silicene layer were offset within

physically reasonable values and the coherent parameters calculated.

3. Results and discussion

3.1. Chemical evidence for a silicon–silver alloy

In figures 1(c) and (d), the (4×4) LEED pattern and the Si 2p core level HR-XPS of (4×4)-silicene are shown. The XP spectrum consists of two spin–orbit doublets, distinguished by a dominant Si $2p_{3/2}$ component at 99.4 eV and the low BE shoulder at 99.1 eV, in a 2.6:1 intensity ratio (high:low BE). A similar XP spectrum has been observed before [13]. Naïvely, based on the accepted buckled (4×4) model [18–21], the higher BE species could be attributed to Si in close proximity to the Ag surface, and the lower BE to more distant Si, with an expected 2:1 ratio for the relative intensities. Silicon nanoribbons on Ag(110) [57, 58] exhibit such a relationship, yet this arises from differing coordination numbers of the Si atoms. Importantly, XPS of silicene on Au(111) and Si nanoribbons on NaCl thin films found only a single Si 2p doublet [59, 60]. Thus, we question the rationale of the chemical shift arising from the intrinsic buckling of the 2D-layer. As will be described below, we instead assign the lower BE component to a Si–Ag alloy species, and the higher BE one to the 2D-Si.

HR-XPS data as a function of Si coverage (figure 2(a)) exhibit a clear evolution of the Si 2p line shape. The relative area ratio of the two doublets varies with coverage and, consequently, cannot simply be explained by two inequivalent Si species within the same structure. Instead, two distinct chemical species must coexist in varying proportion depending on the total coverage. It is important to note that, throughout our spectroscopic studies, we do not have a definitive measure of absolute coverage, and rather our results should be interpreted in terms of relative coverage. However, by inspection of the measured LEED patterns for several preparations, we can, in comparison to the literature, ascribe certain limits to the coverages. By doing so, we assign the highest coverage in figure 2 as 0.4 ML, as described in greater detail in the SI, §3 and figure S2.

At very low Si coverages, the low-BE species dominates the HR-XP spectrum. Only once higher coverages are reached (~0.08 ML) and ordered domains are observed in LEED does the high-BE doublet prevail. This behavior suggests that the low-BE species is the most directly bound to the Ag surface, in direct contravention of the naïve interpretation above, and is established before ordered silicene forms. It is also worth noting that both Si 2p doublets on pristine Ag(111) grow progressively while the Si coverage increases (figure S3), although at differing rates (figure 2(b)), and have been observed in the presence of the (4×4) (figure 1(d)), $\left(\sqrt{13} \times \sqrt{13}\right) R13.9°$ (figure 2(a)) and $\left(2\sqrt{3} \times 2\sqrt{3}\right) R30°$ (figure S5 in SI) phases.

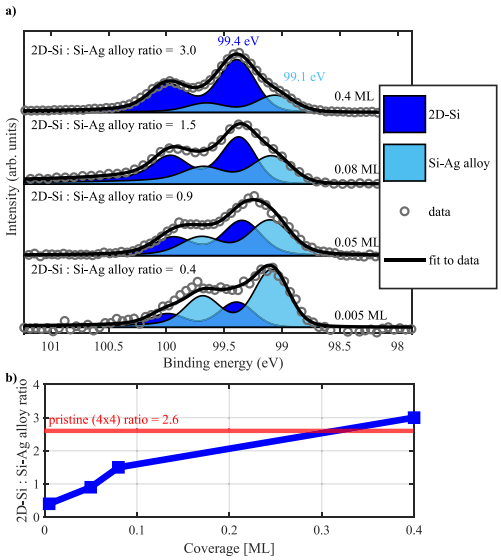

Figure 2. Coverage-dependent evolution of Si 2p HR-XPS of Si/Ag(111). (a) The varying area ratio of the doublets points towards the coexistence of two different surface species. The spectra were normalized to their respective maximum and vertically offset for clarity. The photon energy was 300 eV for the top spectrum, and 250 eV for all the other spectra. Note that, for the 0.08 ML phase, Si 2p XPS was obtained at a photon energy of 300 and 250 eV, and showed no difference in ratio between the two Si components (see figure S4). LEED data of the two topmost coverages are shown in figure S2, for 0.005 ML only the Ag pattern was observed in LEED, while for 0.05 ML LEED was not attempted. (b) Visualization of the 2D-Si: Si–Ag alloy ratio of panel (a). The horizontal red line indicates the ratio of the pristine (4×4) phase (figures 1(c) and (d)), resulting in an extrapolated coverage of roughly 0.3 ML.

We interpret the behavior described above by analogy with the case of germanium on Ag(111). At low coverages, a $GeAg_2$ alloy forms and only at higher coverages does germanene, the Ge analogue to silicene, develop [61]. Ge 3d HR-XPS of the alloy shows a single doublet, which shifts by 0.3 eV to higher BE upon germanene development (SI §7, figure S6). Were the Ge–Si comparison consistent, the lower BE doublet in figures 1 and 2 could be assigned to Si alloyed with Ag (Si–Ag alloy), the higher BE doublet to the 2D-Si layer. Similarly, the Si $2p_{3/2}$ BE of the well-known Si-Cu(111) alloy [62], which exhibits a $\left(\sqrt{3} \times \sqrt{3}\right) R30°$ superstructure, is 98.9 eV (figure 3), similar to the low-BE Si component in the investigated (4×4) phase. Moreover, the Ag $3d_{5/2}$ XP spectrum shown in figure 4 for (4×4)-silicene/Ag(111) exhibits an additional component at higher BE (0.3 eV), which is also suggestive of Ag–Si intermixing and presumably alloying. In fact, a similar Ag $3d_{5/2}$ chemical shift was reported for Sn–Ag alloying [32]. To further support our interpretation, we grew Si on the $GeAg_2$ alloy, resulting in a striking attenuation of the low-BE doublet, relative to

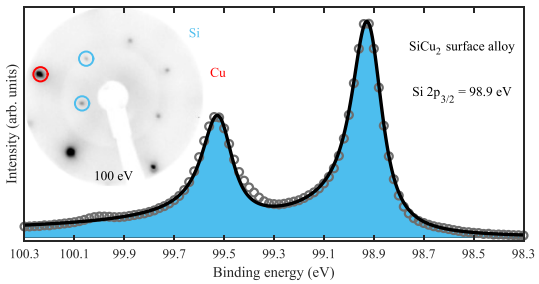

Figure 3. Si 2p XP spectrum of the $SiCu_2$ surface alloy on Cu(111) with the known $\left(\sqrt{3}\times\sqrt{3}\right)R30°$ periodicity [62] (LEED pattern, top-left inset). Similar to figure 2(a)), the binding energy of the surface alloy Si $2p_{3/2}$ component is 98.9 eV. Photon energy: 300 eV.

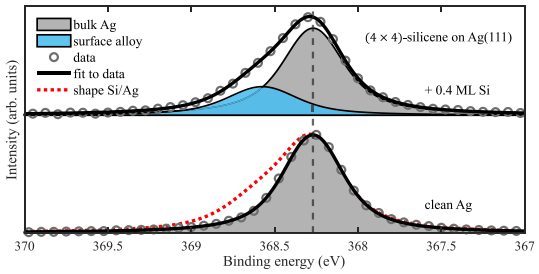

Figure 4. Ag $3d_{5/2}$ XP spectrum of (4×4)-silicene/Ag(111) compared to pristine Ag(111). The Si–Ag alloying is signaled by a high binding energy component fitted in light blue. Photon energy: 435 eV.

the high-BE doublet (figure S7). Such behavior suggests that the $GeAg_2$ alloy can potentially fulfill the role of the low-BE species and thus hinder the Si–Ag alloying.

To test our assumption that the Si–Ag alloy species is enclosed by a 2D-Si layer above it, we exposed both the (4×4)-silicene/Ag(111) layer (shown in figures 1(c) and (d)), as well as a higher coverage layer comprising both (4×4) and $\left(\sqrt{13}\times\sqrt{13}\right)R13.9°$ silicene, to oxygen, namely 100 L (where 1 L, Langmuir, is defined as 10^{-6} mbar s) at RT, and 1200 L at ~473 K, respectively. Silicene is not chemically inert and its oxidation has been reported previously [63–65], however, our XPS study (figure 5) results in a significant reduction of only the higher BE component, which we have assigned to 2D-Si, accompanied by the rise of one or more oxidized Si components at higher BEs. Conversely, the lower BE component remains largely unaffected, hence this phase is hardly oxidized. It seems likely that this component is already in a stable bonding with the Ag substrate and thus is not easily oxidized.

Taken together, all the spectroscopic evidence collected above for silicene in different phases and coverages, as well as oxidized silicene points towards a scenario where an alloy precursor accompanies the growth of 2D-Si at all coverages and is possibly necessary for such growth.

3.2. Testing the accepted honeycomb model and providing structural evidence for the Si–Ag alloy

NIXSW [44] exploits the x-ray standing wavefield created by the interference of incident and reflected waves around the Bragg condition for a given (h,k,l)-reflection. By varying the phase of this standing wave and analyzing the thus modulated photoelectron yield [44], the positional distribution of a species can be determined relative to the Bragg diffraction planes [42]. Ultimately, NIXSW data are reduced to two parameters for each reflection: a coherent fraction (f^{hkl}) and a coherent position (p^{hkl}), which can broadly be considered as the order factor and mean position, respectively, relative to the Bragg diffraction planes. Both parameters take values between 0 and 1, and p^{hkl} is related to the real-space position d by:

$$d = \left(n + p^{hkl}\right) d_{hkl}, \tag{1}$$

with d_{hkl} being the distance between the Bragg diffraction planes, and n an integer value. Note that p^{hkl} of 0 and 1 are equivalent and correspond to an x-ray absorber atom lying on the extrapolated scattering planes. If the scattering planes are parallel to the surface, $n=0$ defines the closest height range above the surface plane, whereas $n=1$ refers to the first extrapolated plane above, etc. Moreover, reflections from planes non-parallel to the surface deliver information on the absorber's lateral registries with respect to the substrate. We acquired Si 1s NIXSW data from the (111) and $(\bar{1}11)$ reflections (figures 6(a)–(d)) after formation of (4×4)-silicene (LEED in figure 1(c)). As with the Si 2p data, the Si 1s core level was deconvoluted into two species (figure S1), Si–Ag alloy and 2D-Si. The respective f^{hkl} and p^{hkl} values are listed in table 1.

For the (111) reflection, probing the adsorption height directly (figure 6(e)), p^{111} is close to 0 (or 1) for both Si components; namely, both species lie, on average, close to either the true ($n=0$) or extrapolated ($n>0$) (111) lattice planes of the substrate. However, both components differ in f^{111}, with f^{111}_{alloy} close to unity and $f^{111}_{\text{2D - Si}}$ around half that value. For the $(\bar{1}11)$ reflection, probing the lateral ordering of the system (figure 6(f)), $p^{\bar{1}11}$ is also found close to zero (or unity) for both species, but compared to their respective f^{111} values, while $f^{\bar{1}11}_{\text{2D - Si}}$ is almost unchanged, $f^{\bar{1}11}_{\text{alloy}}$ is strongly reduced to ~1/3.

The 2D-Si (111) NIXSW results support a buckled film above the surface. Based on LEED-IV, RHEPD, SXRD, STM, AFM and DFT, most studies suggest a honeycomb structure with 18 Si atoms per unit cell, comprising 12 downwards buckled and 6 upwards buckled atoms [11, 18–21, 23, 24, 66–71]. Using 0.06 Å rms vibrational amplitudes (see section 2) and assuming a 2:1 ratio of lower to higher buckled Si atoms, a buckling of 0.87 Å is extracted from the measured $f^{111}_{\text{2D - Si}}$ (primarily probing the structure out of plane). This value agrees well with

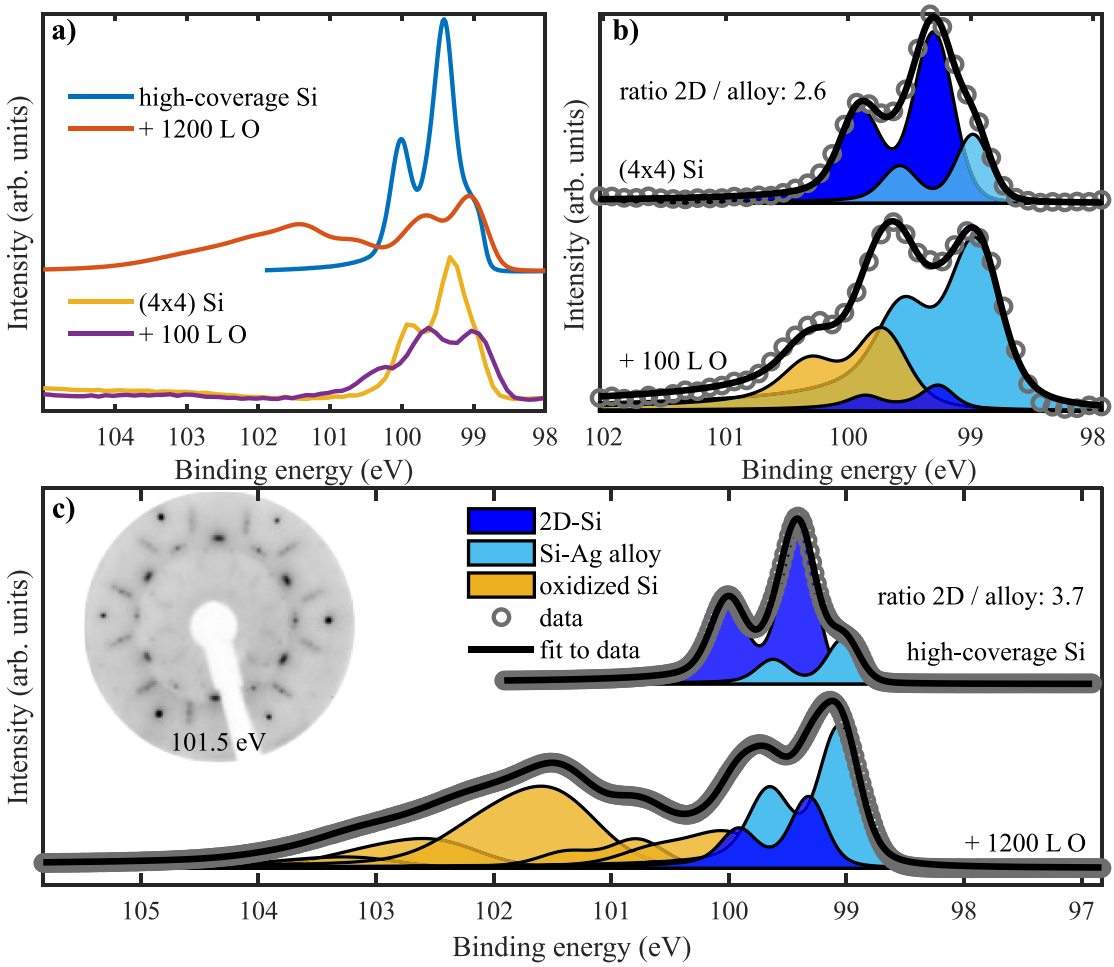

Figure 5. Oxidation of silicene/Ag(111). (a) Area-normalized XPS data of the Si 2p core level for the pristine (4×4)-silicene phase as of figures 1(c) and (d), and after exposure to 100 L of oxygen at RT, and for a higher coverage silicene phase consisting of (4×4) and $\left(\sqrt{13} \times \sqrt{13}\right) R13.9°$ phases, and its exposure to 1200 L of oxygen at a sample temperature of ∼473 K. The data have been normalized to the area of the fitted Si components, background-subtracted and vertically offset for better visibility. Note that, due to different measurement configurations, the XPS intensity between the pristine (4×4) and the high-coverage Si cannot be directly compared. (b) Fit to data for the pristine (4×4)-silicene phase before (replicated from figure 1(d)) and after oxygen exposure. Notably, after exposure only Ag spots were observed in LEED (not shown). (c) Fit to data for the (4×4) and $\left(\sqrt{13} \times \sqrt{13}\right) R13.9°$-silicene phase before and after oxygen exposure. The inset depicts the LEED pattern before oxidation. LEED was not acquired after oxidation. Photon energy: 250 eV.

the range reported in literature (0.75–0.84 Å) [18–21] and corroborates the assignment of this species as 2D-Si. However, as shown in table 1, a simple honeycomb structure, or any model proposed in the literature [11, 18–24, 66–72], cannot explain the determined $f^{\bar{1}11}_{\text{2D - Si}}$ values, sensitive to the lateral registries of the Si atoms.

In this regard, it is worth noting that even considering the Si 1s spectrum as a single peak, i.e. disregarding the need for two distinct features (figures 1(c), 2(a) and S1) and thus assigning the entire Si signal to the silicene layer, would not match the literature models (section 9 of the SI, figure S8 and table S1).

In addition, modifications to this model, e.g. by varying the adsorption height, the buckling, or the lateral position of the rigid silicene layer, do not lead to significant improvements in the agreement with the experimental data (figure S9). Similarly, alternative models, either without buckling [19, 22], including H-atoms [19, 72], or stacking the Si atoms across four sublayers, denoted as (4×4) - β phase [24, 67], cannot reproduce all experimental NIXSW values. Consequently, there is a striking discrepancy between the NIXSW data and the various proposed structures in literature, such that our NIXSW results are incompatible with the generally accepted silicene model. It is important to clarify that the registry of the six upwards buckled atoms is likely incontrovertible, as they can be clearly distinguished by STM or AFM, and our data agree on the apparent size of the reported buckling in height (see above). However, the NIXSW results demand the lateral position of the downwards buckled Si layer needs to be amended.

It is worthwhile to remark that NIXSW is a direct structural methodology and is thus model-independent, hence the measured coherent fraction and coherent position are the structural parameters of the surface that was studied. SXRD, LEED-IV and

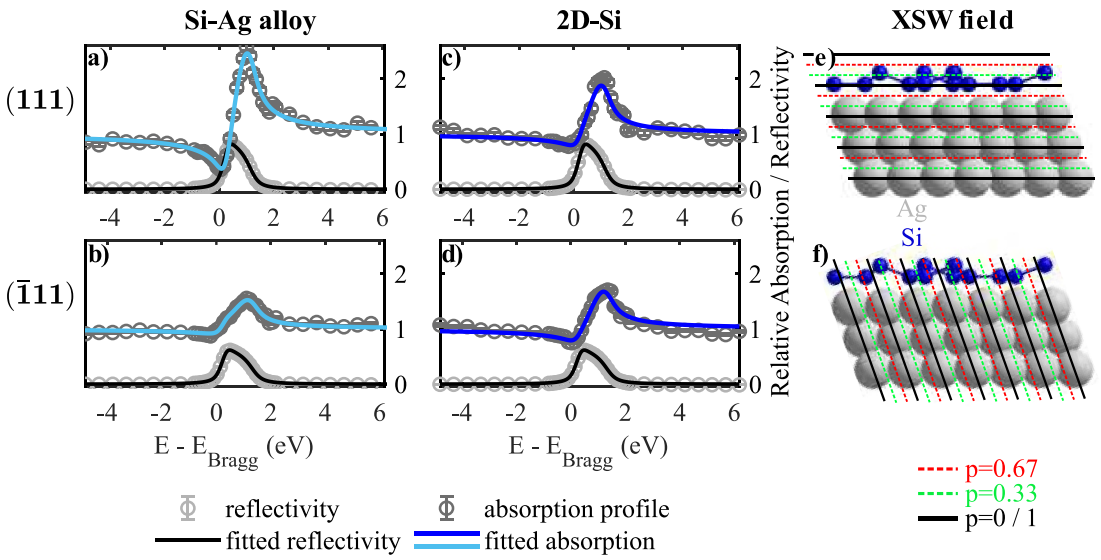

Figure 6. NIXSW absorption profiles of (4×4)-silicene/Ag(111) for quantitative structural analysis. (a), (c) (111) reflection with scattering planes parallel to the surface. (b), (d) $(\bar{1}11)$ reflection with scattering planes inclined by 70.5° with respect to the surface. (a), (b) Si–Ag alloy species. (c), (d) 2D-Si species. The energy scale is defined relative to the Bragg energy. The structural parameters of the fitting are listed in table 1. The respective reflectivity curves (light grey, fitted curves in black) are reported in each panel. (e), (f) Schematics indicating the periodicity of the NIXSW field for the (111) and the $(\bar{1}11)$ reflection, respectively. Si atoms are represented as blue spheres, Ag atoms as grey spheres.

Table 1. Comparison of NIXSW structural parameters for the two spectral species of (4×4)-silicene from the (111) and $(\bar{1}11)$ reflections[a], and calculated DFT structures of published models.

Experiment	f^{111}	p^{111}	Adsorption height (Å)	$f^{\bar{1}11}$	$p^{\bar{1}11}$
Si–Ag alloy (component 1)	0.95 ± 0.04	0.01 ± 0.02	0.00/ 2.36	0.33 ± 0.03	0.94 ± 0.02
2D-Si (component 2)	0.50 ± 0.07	0.97 ± 0.04	$Si_{\uparrow}$[b] : 2.97 $Si_{\downarrow}$[b]: 2.10 (mean : 2.29)	0.51 ± 0.06	0.96 ± 0.03
DFT structure	f^{111}	p^{111}		$f^{\bar{1}11}$	$p^{\bar{1}11}$
Buckled honeycomb [11, 18–21, 23, 24, 66–71]	$0.53 - 0.66$	$0.97 - 0.05$		$0.12 - 0.15$	$0.58 - 0.61$
(4×4) - β honeycomb [24, 67]	0.59	0.99		0.09	0.55
Non-buckled honeycomb [19, 22]	1.00	0.95		0.01	0.40
Hydrogenated honeycomb [19, 72]	0.79 (1.00)[c]	0.99 (0.95)[c]		0.13 (0.19)[c]	0.84 (0.32)[c]

[a] Note that a coherent position (p) of 0 is equivalent to 1; a coherent fraction (f) of 1 indicates perfect order; the (111) reflection is only sensitive to the height of the given species above the surface; the $(\bar{1}11)$ reflection is also sensitive to the lateral periodicity.

[b] $Si_{\uparrow}$ and $Si_{\downarrow}$ are defined schematically in figure 1(b).

[c] DFT-relaxation resulted in a significant change in structure of this model from the starting values, the numbers in brackets are those of the unrelaxed published structure.

RHEPD, in contrast, all require an approach with a series of trial-and-error modeling to arrive at the correct structure. In other words, these techniques, like DFT, will never converge on the correct structure if they are not provided with the correct base structure. As such, they are 'imagination limited' and, as there was no prior expectation of a Si–Ag alloy, its inclusion in the modeling of the SXRD, LEED-IV and RHEPD data would have been counter-intuitive. In view of our work, a reanalysis of these data, including a Si–Ag alloy, would be illuminating. While NIXSW cannot be used to determine the whole structure directly, as can be achieved with SXRD and LEED-IV, the true structure must possess the same coherent fractions and coherent positions as measured by NIXSW. NIXSW, however, unlike SXRD and LEED-IV will probe all Si atoms on the surface, rather than being dominated by those present in the ordered overlayer. As such NIXSW cannot differentiate between the (4×4) overlayer and any notable secondary overlayer

on the surface, which could be the origin of the discrepancy between NIXSW and the structures from the published models, but, as discussed later in this article, we do not believe that this is likely. Nor can NIXSW tell us that the Si–Ag alloy is present in the (4×4) mesh, for that we turn to STM in the following section.

For the Si–Ag alloy, the high f^{111}_{alloy} suggests that all atoms of this species lie at a similar height. Therefore, it is important to understand whether this height is equiplanar with the Ag surface atoms ($n = 0$) or adsorbed above the surface ($n \geqslant 1$)? As this species grows first on the surface (as described above), it is unlikely that it lies significantly above the 2D-Si film, excluding the case $n > 1$. Similarly, if $n = 1$, the Si–Ag alloy species would lie on the surface at an adsorption height roughly in the middle of the 2D-Si buckling, assuming $n_{\text{2D - Si}} = 1$. While this is not *a priori* impossible, it is hard to rationalize why Si atoms that differ in height by 0.87 Å would exhibit no BE shift, yet a species that lies between them would be shifted by ∼0.3 eV. Therefore, the simplest conclusion is $n = 0$, i.e. this species is indeed incorporated into the surface layer of silver at the same out-of-plane height as the Ag atoms, forming a Si–Ag alloy.

The low $f^{\bar{1}11}_{\text{alloy}}$ value, on the other hand, excludes that this alloy is purely substitutional, which would result in a $f^{\bar{1}11}_{\text{alloy}}$ value close to unity (see in the SI: §11,12, incl. tables S2, S3 and figures S10–S16). In particular, considering high-symmetry sites for the Si occupation, only a mixture of substitutional and surface bridge sites would match the data satisfactorily (table S2, figure S10).

In summary, not only does NIXSW exclude all literature-proposed structural models, but also strongly underpins the presence of a substantial Si alloy species that is co-planar with substrate Ag atoms.

3.3. Discovery of a new phase of potentially pure Si–Ag alloy

As discussed above, the Si–Ag alloy species is the dominant phase at low coverages, thus an extensive STM study in the sub-ML coverage regime was performed to try and identify its origin. At ultra-low Si-coverages (≪0.1 ML), where ordered silicene phases have not yet developed, Si atoms aggregate into small clusters and islands that contrast darkly on the Ag terraces. With increasing coverage, these regions grow in size and partially feature a local ordering of hexagonal rings, as shown in figure 7(a), before a well-defined extended hexagonal pattern emerges (figure 7(b)). This phase cannot be attributed to any of the known silicene superstructures published to date. Note that isolated Si adatoms were not detected in the wide range of investigated coverages. At Si coverages in the ∼0.1 ML range, ordered silicene phases begin to form (figure 7(c)). Occasionally (<10%), at these coverages, the same novel motif shown in figures 7(a) and (b) was found neighboring (4×4) islands (figures 7(c) and S17–S19). Above 0.3 ML this new phase is no longer observed, and increasing Si deposition only extends the size of the (4×4) islands and leads to the formation of additional silicene superstructures (e.g. $\left(\sqrt{13} \times \sqrt{13}\right) R13.9°$ or $\left(2\sqrt{3} \times 2\sqrt{3}\right) R30°$) [21].

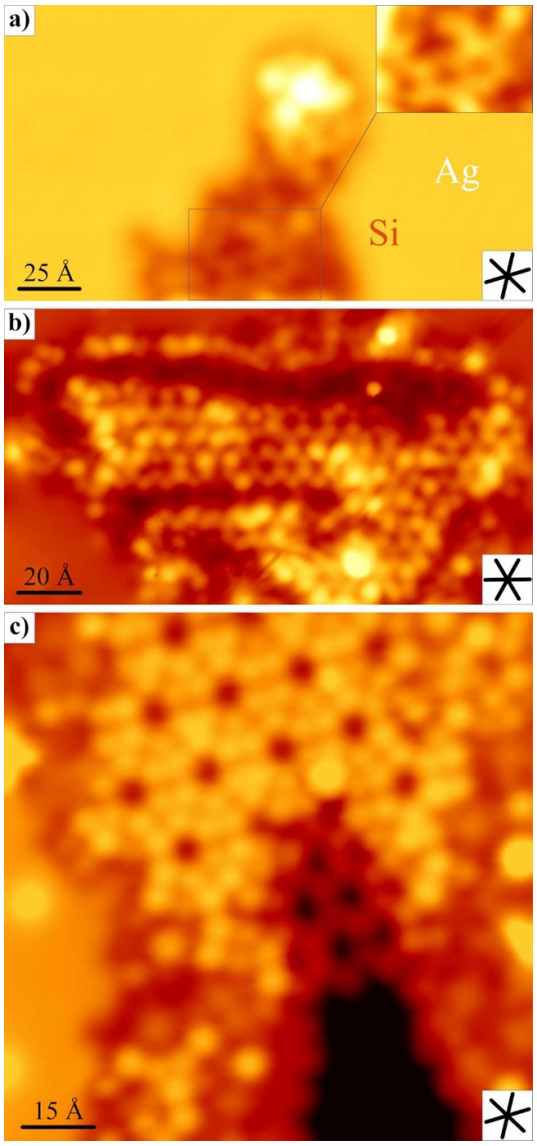

Figure 7. (a)–(c) High-resolution STM evidence of new phase of potentially pure Si–Ag alloy. Previously unreported phase of Si assembly on Ag(111) without (a), (b) and with (c) adjoining (4×4)-silicene. The same periodicity of this novel phase is revealed at different Si coverages (figure S17). (a) Low coverage (<0.05 ML): Si forms isolated islands with local ordering that follows the Ag closed-packed directions (black lines). The inset has a modified contrast to highlight this newly discovered phase. (b), (c) Higher coverage (∼0.1 ML): the local ordered Si islands grow in size (b) and the (4×4) superstructure develops, occasionally (<10%) revealing the novel phase at the border with a Ag step edge (c), also see figures S18 and S19. In (a)–(c), the length of the repeating unit of this phase is 7.5 ± 0.4 Å. Imaging parameters: (a) 133×75 Å^2, 1.20 V, 0.07 nA; (b) 156×88 Å^2, −0.05 V, 0.07 nA; (c) 78×78 Å^2, −0.25 V, 0.10 nA.

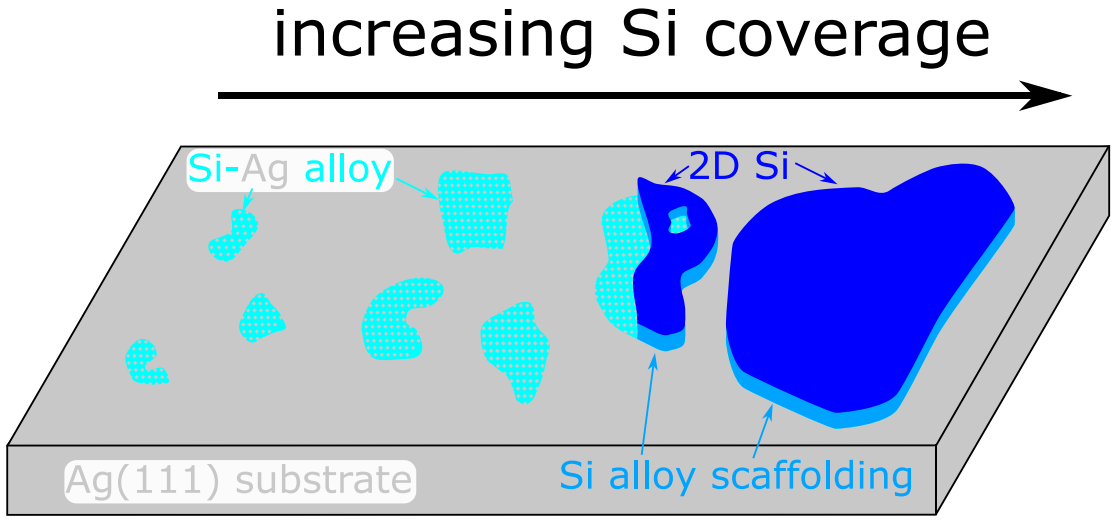

Figure 8. Schematic model of (4×4)-silicene growth. At low coverages, a Si–Ag surface alloy forms, providing the basis for 2D-Si growth at intermediate coverages. At high coverages, the surface is covered with 2D-Si, while the Si–Ag alloy persists, as scaffold for the stabilization of the 2D-Si.

This newly discovered phase is discussed in greater detail in section 13 of the SI, and is characterized by a repeating unit of the hexagonal structure of 7.5 ± 0.4 Å. Were such repeating unit the true unit cell of this phase, it would correspond to a $(2.6 \pm 0.2 \times 2.6 \pm 0.2)$ superstructure on the Ag(111), see figure S18. The repeating unit of the rings in the STM of this novel phase are 35% smaller than the (4×4) phase. Since this novel phase appears predominantly at low coverage, which according to our coverage-dependent HR-XPS is dominated by the Si–Ag alloy species (figure 2(a)), we propose that this phase is a pure Si–Ag alloy. This assignment is consistent with the lower apparent height of this phase in the STM measurements, as shown in figure S19, and suggests that the pure Si–Ag alloy phase does not simply occupy substitutional Ag sites in the Ag(111) surface (unlike the other group IV alloys), as the NIXSW results indicate. Instead, the Si–Ag alloy is more densely packed and must reconstruct or strain the Ag(111) surface.

Importantly, we only observed this phase either before formation of (4×4) domains (figures 7(a) and (b)), emanating from the (4×4) phase (figures 7(c) and S19) or within (4×4) domains (figure S17). This finding strongly suggests that it is a precursor from which the (4×4) structure grows. In other words, not only is the Si–Ag alloy species present in the (4×4) phase, but this alloy also acts as a scaffold from which the silicene grows. Moreover, it is important to note that, at no point did we ever observe large domains of this $(2.6 \pm 0.2 \times 2.6 \pm 0.2)$ phase in the STM, nor were any additional spots observed in the LEED data, pointing towards this newly discovered phase being intrinsically limited in size. This could indicate that the Si–Ag alloy exhibits significant strain due to the apparent large mismatch in the period of the repeating unit and the underlying substrate, thus once a certain size limit is reached it may be far more energetically favorable to grow 2D-Si on top of the Si–Ag alloy, than to expand the pure Si–Ag alloy precursor phase. We extrapolate, that the Si–Ag alloy is altered into a (4×4)-phase, when this threshold coverage is reached. The observed behavior is in distinct contrast to the other Group IV alloys with Ag, where large, ordered alloy islands are observed in both STM [31–33, 73, 74] and LEED (figure S6(d)). Moreover, in the germanium case, 2D-growth begins to occur once a high coverage of the alloy is achieved and dealloying takes place (figure S6). Here, instead, as soon as the 2D-Si begins to grow, expansion of the Si islands results in both the 2D-Si and Si–Ag alloy growing concomitantly (figure 2).

Finally, DFT simulations of STM images for Si alloy atoms in substitutional sites indicate comparatively minor changes to the expected appearance in the majority of cases (SI, §12), and all bear a striking resemblance to similar such calculations for the current literature model of (4×4) silicene [75, 76]. It is indeed unlikely many authors would fail to ascribe good agreement between the various simulated STM images in figure S13 and the STM data present in the literature, which highlights the danger in assigning structural motifs by STM and DFT alone [77].

3.4. What the alloy must look like

It is important to recognize that the only phase present in the LEED shown in figure 1(c) corresponds to a (4×4) superstructure. Thus, the Si–Ag alloy species must either be composite with the 2D-Si species in the (4×4) islands or only be present in phases that are either too disordered or too small to be seen in LEED. While, at very low coverages, STM indicates the presence of poorly ordered Si

phases, once the (4×4) islands (and other known phases) begin to grow, the boundaries between silicene and Ag are clearly established without disordered areas in-between. The only other observed phase is the newly discovered $(2.6 \pm 0.2 \times 2.6 \pm 0.2)$ phase, which is always in minority on the surface ($\ll$10%) and was only ever observed at low Si coverages (<0.3 ML). Thus, at the investigated coverage of the (4×4) phase (figures 1(c) and (d)) the HR-XPS and NIXSW measurements should be almost entirely dominated by the (4×4) phase. Yet the HR-XPS/NIXSW measurements indicate that a substantial proportion of Si atoms are alloyed with silver. Therefore, the combination of our HR-XPS, NIXSW and STM results all lead to a single conclusion: a Si–Ag alloy is part of the (4×4) phase and must lie beneath the 2D-Si film. Thus, in the context of the (4×4) phase, what do we know of the physical properties of the Si–Ag alloy?

From the NIXSW measurements, we estimate that there are ∼3 2D-Si atoms per 2 Si alloy atoms (SI, §14). Thus, assuming 18 Si atoms in the 2D-Si layer as in the honeycomb model, this would amount to about 12 Si alloy atoms below the (4×4) cell. This high Si:Ag ratio in the first layer may indicate that the Si–Ag alloy is not just present at the surface but potentially extends into sub-surface Ag layers, though it is important to highlight that stoichiometric assignments from XPS have a significant associated uncertainty. Additionally, the NIXSW results from the $(\bar{1}11)$ reflection, and the newly discovered $(2.6 \pm 0.2 \times 2.6 \pm 0.2)$ phase, both point towards the Si atoms in the alloy not simply occupying substitutional Ag sites. In particular, NIXSW data suggest a mixture of substitutional and bridge sites. It seems likely that the Si alloy atoms interact with the 2D-Si atoms, preventing decoupling of this layer from the Ag(111) substrate. This would also agree with the introductory remarks about the strong interaction of silicene with the Ag substrate, invoked to justify both the appearance [15] and the absence [12, 16, 17] of the Dirac cone structure.

Deductively, the presence of this Si–Ag alloy would mean that Si on Ag(111) behaves similarly to Ge and Sn: at low coverages a surface alloy is formed, which provides the basis for the 2D phase at higher coverages. However, while Ge de-alloys completely [61], the Si–Ag alloy would pervasively persist at higher coverages, providing the basis for the stabilization of silicene on top, similarly to the stanene growth on $SnAg_2$ [32]. Hence, the Si–Ag alloy may act as both scaffold and foundation for the 2D-Si film, as schematically depicted in figure 8.

4. Conclusions

We have presented a multi-faceted investigation of the most studied silicene phase, (4×4)-silicene on Ag(111). The presented experimental results are incompatible with the generally accepted (4×4) honeycomb model, instead indicating the additional presence of a pervasive Si surface alloy, located beneath the 2D-Si layer. The Si–Ag alloy exhibits a characteristic fingerprint in both HR-XPS and NIXSW, with an energy shift towards lower BEs relative to the non-alloyed atoms and in good agreement with Si/Cu(111) and Ge/Ag(111) alloys. The NIXSW analysis shows that the silicene layer is significantly buckled, with a buckling of about 0.87 Å, agreeing well with previous structural studies and DFT calculations. However, the XSW results cannot be reconciled with the honeycomb-like models found in the literature, which would all yield considerably lower coherent fractions from the $(\bar{1}11)$ Bragg reflection. In STM, at intermediate and high Si coverages, the (4×4)-silicene does not coexist with any other separate phase, ordered or disordered, and LEED indicates the exclusive presence of a (4×4) superstructure on the surface. We therefore infer that the Si–Ag alloy must lie below the 2D-Si layer, although its structure remains elusive.

Furthermore, the evidence of alloying implies that previous studies into silicene's electronic structure must be reconsidered, as interaction with underlying Si will certainly alter the conduction and valence bands of the silicene [78]. It is even questionable whether the 2D-Si can be regarded as 2D material at all, as it would be making strong chemical bonds well outwith the 2D plane that defines the layer. Finally, the role that we propose for the Si–Ag alloy in the growth of silicene, and the role that the Ge–Ag, Sn–Ag and Sn–Au alloys play in the growth of germanene and stanene [32, 61, 79], suggest that the alloy scaffolding of 2D materials may be a common phenomenon on metal surfaces and have implications for delaminating these films from their growth substrate, which has been achieved for hydrogenated and oxidized silicene and gemanene [80]. Ultimately, silicene on Ag(111) may have more in common with Ca intercalated Si or Ge [81, 82], than ideal freestanding silicene. Elucidating the interaction between such alloy phases and the 2D-layer is crucial for understanding the manifestation of strong interfacial interactions, which profoundly affect the electronic structure of silicene, and to control the growth and properties of these films.

Data availability statement

The data that support the findings of this study are available upon reasonable request from the authors.

Acknowledgments

J T K acknowledges funding from the Konrad-Adenauer-Stiftung (KAS). This work was supported by the Deutsche Forschungsgemeinschaft (DFG) through the TUM International Graduate School of Science and Engineering (IGSSE), GSC 81, the

e-conversion Cluster of Excellence, and a Heisenberg Professorship (W A), and by the European Research Council Consolidator Grant NanoSurfs (No. 615233). D A D acknowledges funding from the Marie Curie Intra-European Fellowship (FP7, 626397—SiliNano). We acknowledge the Diamond Light Source for the award of synchrotron beamtime (SI15804-1, SI20771-1) and would like to thank Dave McCue and Pardeep Thakur Kumar for assistance. We also acknowledge the Paul Scherrer Institut, Villigen, Switzerland for provision of synchrotron radiation beamtime at beamline X03DA (PEARL) of the SLS and would like to thank Patrick Ascher and Nicolas Bachellier for assistance. We thank Keitaro Eguchi, Peter Knecht and Reza Kakavandi for experimental support.

Author contributions

D A D, F A, J V B and P F conceived the idea. D A D, F A and W A designed the experiments and supervised the project. J T K performed all measurements and data analysis with strong support from A B. A P S performed the DFT calculations. J T K, A B, D A D, F A, M S, F H, P T P R, M M, P P and T L L conducted the synchrotron beamtimes at SLS and Diamond Light Source. All authors participated in the scientific discussion and contributed in the writing based on the draft written by J T K, A B, D A D and F A.

Conflict of interest

The authors declare no competing financial interest.

ORCID iDs

Matthias Muntwiler https://orcid.org/0000-0002-6628-3977
Johannes V Barth https://orcid.org/0000-0002-6270-2150
Willi Auwärter https://orcid.org/0000-0001-9452-4662
David A Duncan https://orcid.org/0000-0002-0827-2022
Francesco Allegretti https://orcid.org/0000-0001-6141-7166

References

[1] Zhou S Y, Gweon G H, Fedorov A V, First P N, de Heer W A, Lee D H, Guinea F, Castro Neto A H and Lanzara A 2007 *Nat. Mater.* **6** 770–5
[2] Rotenberg E, Bostwick A, Ohta T, McChesney J L, Seyller T and Horn K 2008 *Nat. Mater.* **7** 258–9
[3] Balog R *et al* 2010 *Nat. Mater.* **9** 315–9
[4] Xu X, Liu C, Sun Z, Cao T, Zhang Z, Wang E, Liu Z and Liu K 2018 *Chem. Soc. Rev.* **47** 3059–99
[5] Drummond N D, Zólyomi V and Fal'ko V I 2012 *Phys. Rev.* B **85** 075423
[6] Ni Z, Liu Q, Tang K, Zheng J, Zhou J, Qin R, Gao Z, Yu D and Lu J 2012 *Nano Lett.* **12** 113–8
[7] Molle A, Grazianetti C, Tao L, Taneja D, Alam M H and Akinwande D 2018 *Chem. Soc. Rev.* **47** 6370–87
[8] Lalmi B, Oughaddou H, Enriquez H, Kara A, Vizzini S, Ealet B and Aufray B 2010 *Appl. Phys. Lett.* **97** 223109
[9] Jamgotchian H, Colignon Y, Hamzaoui N, Ealet B, Hoarau J Y, Aufray B and Bibérian J P 2012 *J. Phys.: Condens. Matter* **24** 172001
[10] Oughaddou H, Enriquez H, Tchalala M R, Yildirim H, Mayne A J, Bendounan A, Dujardin G, Ait Ali M and Kara A 2015 *Prog. Surf. Sci.* **90** 46–83
[11] Vogt P, De Padova P, Quaresima C, Avila J, Frantzeskakis E, Asensio M C, Resta A, Ealet B and Le Lay G 2012 *Phys. Rev. Lett.* **108** 155501
[12] Mahatha S K, Moras P, Bellini V, Sheverdyaeva P M, Struzzi C, Petaccia L and Carbone C 2014 *Phys. Rev.* B **89** 201416
[13] Du Y *et al* 2016 *Sci. Adv.* **2** e1600067
[14] Gori P, Pulci O, Ronci F, Colonna S and Bechstedt F 2013 *J. Appl. Phys.* **114** 113710
[15] Feng Y *et al* 2016 *Proc. Natl Acad. Sci. USA* **113** 14656–61
[16] Mahatha S K, Moras P, Sheverdyaeva P M, Bellini V, Menteş T O, Locatelli A, Flammini R, Horn K and Carbone C 2017 *J. Electron Spectrosc. Relat. Phenom.* **219** 2–8
[17] Sheverdyaeva P M, Mahatha S K, Moras P, Petaccia L, Fratesi G, Onida G and Carbone C 2017 *ACS Nano* **11** 975–82
[18] Fukaya Y, Mochizuki I, Maekawa M, Wada K, Hyodo T, Matsuda I and Kawasuso A 2013 *Phys. Rev.* B **88** 205413
[19] Kawahara K, Shirasawa T, Arafune R, Lin C-L, Takahashi T, Kawai M and Takagi N 2014 *Surf. Sci.* **623** 25–28
[20] Curcella A, Bernard R, Borensztein Y, Resta A, Lazzeri M and Prévot G 2016 *Phys. Rev.* B **94** 165438
[21] Pawlak R, Drechsel C, D'Astolfo P, Kisiel M, Meyer E and Cerda J I 2020 *Proc. Natl Acad. Sci. USA* **117** 228–37
[22] Cahangirov S, Topsakal M, Aktürk E, Şahin H and Ciraci S 2009 *Phys. Rev. Lett.* **102** 236804
[23] Lin C-L, Arafune R, Kawahara K, Tsukahara N, Minamitani E, Kim Y, Takagi N and Kawai M 2012 *Appl. Phys. Express* **5** 045802
[24] Guo Z-X, Furuya S, Iwata J-I and Oshiyama A 2013 *Phys. Rev.* B **87** 235435
[25] Mannix A J, Kiraly B, Fisher B L, Hersam M C and Guisinger N P 2014 *ACS Nano* **8** 7538–47
[26] Bocîrnea A E, Costescu R M, Apostol N G and Teodorescu C M 2019 *Appl. Surf. Sci.* **473** 433–41
[27] Curcella A, Bernard R, Borensztein Y, Lazzeri M and Prévot G 2018 *Nanoscale* **10** 2291–300
[28] Sone J, Yamagami T, Aoki Y, Nakatsuji K and Hirayama H 2014 *New J. Phys.* **16** 095004
[29] Prévot G, Bernard R, Cruguel H and Borensztein Y 2014 *Appl. Phys. Lett.* **105** 213106
[30] Oughaddou H *et al* 2000 *Phys. Rev.* B **62** 16653–6
[31] Dalmas J, Oughaddou H, Léandri C, Gay J-M, Le Lay G, Tréglia G, Aufray B, Bunk O and Johnson R L 2005 *Phys. Rev.* B **72** 155424
[32] Yuhara J, Fujii Y, Nishino K, Isobe N, Nakatake M, Xian L, Rubio A and Le Lay G 2018 *2D Mater.* **5** 025002
[33] Osiecki J R and Uhrberg R I G 2013 *Phys. Rev.* B **87** 075441
[34] Bernard R, Borensztein Y, Cruguel H, Lazzeri M and Prévot G 2015 *Phys. Rev.* B **92** 045415
[35] Satta M, Colonna S, Flammini R, Cricenti A and Ronci F 2015 *Phys. Rev. Lett.* **115** 026102
[36] Prévot G, Bernard R, Cruguel H, Curcella A, Lazzeri M, Leoni T, Masson L, Ranguis A and Borensztein Y 2016 *Phys. Status Solidi* b **253** 206–17
[37] Moras P, Mentes T O, Sheverdyaeva P M, Locatelli A and Carbone C 2014 *J. Phys.: Condens. Matter* **26** 185001
[38] Muntwiler M *et al* 2017 *J. Synchrotron Radiat.* **24** 354–66
[39] Avila J, De Padova P, Cho S, Colambo I, Lorcy S, Quaresima C, Vogt P, Resta A, Le Lay G and Asensio M C 2013 *J. Phys.: Condens. Matter* **25** 262001

[40] Leandri C, Lay G L, Aufray B, Girardeaux C, Avila J, Dávila M E, Asensio M C, Ottaviani C and Cricenti A 2005 *Surf. Sci.* **574** L9–L15
[41] Lee T-L and Duncan D A 2018 *Synchrotron Radiat. News* **31** 16–22
[42] Bedzyk M J and Materlik G 1985 *Phys. Rev.* B **32** 6456–63
[43] Batterman B W and Cole H 1964 *Rev. Mod. Phys.* **36** 681–717
[44] Woodruff D P 2005 *Rep. Prog. Phys.* **68** 743–98
[45] Fisher C J, Ithin R, Jones R G, Jackson G J, Woodruff D P and Cowie B C C 1998 *J. Phys.: Condens. Matter* **10** L623–L9
[46] Woodruff D P and Duncan D A 2020 *New J. Phys.* **22** 113012
[47] Hohenberg P and Kohn W 1964 *Phys. Rev.* **136** B864–B71
[48] Hamada I 2014 *Phys. Rev.* B **89** 121103
[49] Schulz F, Liljeroth P and Seitsonen A P 2019 *Phys. Rev. Mater.* **3** 084001
[50] Monkhorst H J and Pack J D 1976 *Phys. Rev.* B **13** 5188–92
[51] Blöchl P E 1994 *Phys. Rev.* B **50** 17953–79
[52] Tersoff J and Hamann D R 1985 *Phys. Rev.* B **31** 805–13
[53] Giannozzi P *et al* 2009 *J. Phys.: Condens. Matter* **21** 395502
[54] Thonhauser T, Cooper V R, Li S, Puzder A, Hyldgaard P and Langreth D C 2007 *Phys. Rev.* B **76** 125112
[55] Dal Corso A 2014 *Comput. Mater. Sci.* **95** 337–50
[56] Kresse G and Hafner J 1993 *Phys. Rev.* B **47** 558–61
[57] Cerdá J I, Sławińska J, Le Lay G, Marele A C, Gómez-Rodríguez J M and Dávila M E 2016 *Nat. Commun.* **7** 13076
[58] Espeter P, Keutner C, Roese P, Shamout K, Berges U, Wenzel G, Bignardi L, Kleimeier N F, Zacharias H and Westphal C 2017 *Nanotechnology* **28** 455701
[59] Sadeddine S, Enriquez H, Bendounan A, Kumar Das P, Vobornik I, Kara A, Mayne A J, Sirotti F, Dujardin G and Oughaddou H 2017 *Sci. Rep.* **7** 44400
[60] Quertite K *et al* 2021 *Adv. Funct. Mater.* **31** 2007013
[61] Lin C *et al* 2018 *Phys. Rev. Mater.* **2** 024003
[62] Shuttleworth I G, Fisher C J, Lee J J, Jones R G and Woodruff D P 2001 *Surf. Sci.* **491** L645–L50
[63] Molle A, Grazianetti C, Chiappe D, Cinquanta E, Cianci E, Tallarida G and Fanciulli M 2013 *Adv. Funct. Mater.* **23** 4340–4
[64] Xu X *et al* 2014 *Sci. Rep.* **4** 7543
[65] Solonenko D, Selyshchev O, Zahn D R T and Vogt P 2019 *Phys. Status Solidi* b **256** 1800432
[66] Arafune R, Lin C-L, Kawahara K, Tsukahara N, Minamitani E, Kim Y, Takagi N and Kawai M 2013 *Surf. Sci.* **608** 297–300
[67] Liu Z L, Wang M-X, Xu J-P, Ge J-F, Lay G L, Vogt P, Qian D, Gao C-L, Liu C and Jia J-F 2014 *New J. Phys.* **16** 075006
[68] Enriquez H, Vizzini S, Kara A, Lalmi B and Oughaddou H 2012 *J. Phys.: Condens. Matter* **24** 314211
[69] Pflugradt P, Matthes L and Bechstedt F 2014 *Phys. Rev.* B **89** 035403
[70] Onoda J, Yabuoshi K, Miyazaki H and Sugimoto Y 2017 *Phys. Rev.* B **96** 241302
[71] Gao J and Zhao J 2012 *Sci. Rep.* **2** 861
[72] Feng B, Ding Z, Meng S, Yao Y, He X, Cheng P, Chen L and Wu K 2012 *Nano Lett.* **12** 3507–11
[73] Deng J, Ablat G, Yang Y, Fu X, Wu Q, Li P, Zhang L, Safaei A, Zhang L and Qin Z 2021 *J. Phys.: Condens. Matter* **33** 225001
[74] Chen T Y, Mikolas D, Chiniwar S, Huang A, Lin C-H, Cheng C-M, Mou C-Y, Jeng H-T, Pai W W and Tang S-J 2021 *Phys. Revi. Res.* **3** 033138
[75] Cahangirov S, Audiffred M, Tang P, Iacomino A, Duan W, Merino G and Rubio A 2013 *Phys. Rev.* B **88** 035432
[76] Guerrero-Sánchez J, Munoz-Pizza D M and Takeuchi N 2019 *Appl. Surf. Sci.* **479** 847–51
[77] Woodruff D P 2019 *Jpn. J. Appl. Phys.* **58** 100501
[78] Restrepo O D, Mishra R, Goldberger J E and Windl W 2014 *J. Appl. Phys.* **115** 033711
[79] Zhou D *et al* 2021 *J. Phys. Chem. Lett.* **12** 211–7
[80] Bianco E, Butler S, Jiang S, Restrepo O D, Windl W and Goldberger J E 2013 *ACS Nano* **7** 4414–21
[81] Terada T, Uematsu Y, Ishibe T, Naruse N, Sato K, Nguyen T Q, Kobayashi E, Nakano H and Nakamura Y 2022 *Adv. Mater. Interfaces* **9** 2101752
[82] Uematsu Y, Terada T, Sato K, Ishibe T and Nakamura Y 2020 *Appl. Phys. Express* **13** 055503